Int. J. Multiphase Flow Vol. 12, No. 3, pp. 405–425, 1986
Printed in Great Britain

0301–9322/86 $3.00 + .00
Pergamon Journals/Elsevier

MEASUREMENT OF PHASE DISTRIBUTION IN A TRIANGULAR CONDUIT

SUK K. SIM
Reactor Design Division, Combustion Engineering, Inc., Windsor, CT 06095, U.S.A.

RICHARD T. LAHEY, JR.
Department of Nuclear Engineering, RPI, Troy, NY 12181, U.S.A.

(*Received* 12 *November* 1984; *in revised form* 20 *August* 1985)

Abstract—Measurements of phase-distribution phenomena were made for fully developed, turbulent air/water two-phase flow in a vertical isosceles-triangular test section. These measurements included the local void-fraction and liquid-phase velocity using an RF-excited local impedance probe and Pitot tube, respectively. It was found that substantial lateral "void drift" occurred, with the vapor phase collecting in the more open, high-velocity, region of the test section.

INTRODUCTION

Most previous experimental and analytical investigations of two-phase flow have concentrated on one-dimensional effects rather than the multidimensional effects exhibited by two-phase flow. This, however, does not imply that transverse phase-distribution phenomena has not been recognized as being important; rather it is a reflection of the difficulty involved in measuring and predicting these phenomena.

The literature reveals that when transverse phase-distribution mechanisms play an important role, they have normally been taken into account by the application of experimentally derived correlations or correction factors. Unfortunately, such correlations or correction factors are normally restricted to specific geometries and flow conditions.

One of the most important aspects of two-phase structure is the transverse phase distribution which occurs. Indeed, the lateral-phase distribution is often of primary importance in heat transfer and fluid flow analyses in the chemical process and power industries. Beattie (1972) has derived void profiles based on a simple momentum balance and an empirical relation between the local void-fraction and local liquid-phase axial velocity. Ishii (1975) has formulated a three-dimensional model of two-phase flow by considering each phase separately. Drew & Lahey (1981) have solved the equations of Ishii and derived an analytical model of lateral-phase distribution for the case of fully developed, adiabatic, steady turbulent two-phase flow in a circular tube. Drew & Lahey (1981) have further extended this model to noncircular geometry and derived an analytical model for the lateral-phase distribution mechanisms in fully developed, turbulent two-phase flow in channels of arbitrary cross-sections. It has been found that for bubbly flow, it is the distribution of the liquid-phase turbulence (and thus the local pressure) which determines the lateral void distribution. Furthermore, the void distribution depends on the anisotropic nature of the turbulent two-phase flow.

In an experimental study, Serizawa *et al.* (1974) made detailed measurements in axisymmetric turbulent two-phase air/water flow in a circular pipe. He found that, for low-quality two-phase flow, the bubbles collected near the wall, where the liquid-phase turbulence was the highest. Lance *et al.* (1980) measured the turbulent structure of a cocurrent air/water bubbly two-phase mixture flowing upward in a vertical rectangular channel. It was found that the bubbles responded to, and modify, the structure of liquid-phase turbulence. Lahey *et al.* (1971) made detailed steam/water subchannel measurements in a heated rod bundle. They found a pronounced degree of lateral-phase separation, with the vapor flowing preferentially in the larger subchannels. Based on these data, a lateral "void-drift" model was proposed.

As isosceles-triangular duct was used in this study. Such a test section allows for complex flow structure and phase distribution in a relatively simple geometry and has been

used widely in single-phase flow measurements, e.g. Nikuradse (1926), Eckert *et al.* (1956) and Aly *et al.* (1978). In order to understand the multidimensional phase-distribution mechanisms involved, the void-fraction and liquid-phase velocity distributions were measured for fully developed, turbulent air/water flow using both a Radio Frequency (RF)-excited local impedance probe and a Pitot tube. A single-beam gamma densitometer was used to measure the chordal-average void fraction and was used as a standard for the measured local void fraction.

DESCRIPTION OF THE EXPERIMENTAL FACILITY AND MEASURING SYSTEM

Air/water loop

A large air/water loop, shown in figure 1, was used in this study. This loop was designed to be used to perform experiments with various test sections in order to understand phase separation and distribution phenomena in flowing two-phase systems. As noted above, an isosceles-triangular test section was used in this study.

The water portion of the loop is a closed system in which the water is stored in a water collection tank and moved through the loop by a centrifugal pump. From the water-collection tank, the water flows downward into the suction side of the centrifugal pump, which is rated for 265 l/m. After leaving the pump, part of the flow is diverted through a filtering element and returned back to the collection tank. The remainder passes through a mixing tee, where it is combined with compressed air to achieve a two-phase flow. Before the entrance of the mixing tee, a globe valve controls the required water-flow rate which is measured with a calibrated orifice meter. At the lowest point on the water side of the loop there is a drain valve, so that the loop can be drained at the end of each day's experiments. All water lines were made of 3.81-cm-diam. copper tubing. The heat absorbed by the water, due to frictional pressure losses and pump work, is removed by a heat exchanger (copper coil) installed in the water-collection tank.

The compressed air source is a positive displacement air compressor. This compressor is rated for about 3 m^3/min of air at 6.9 bars.

The compressed air passes through an oil separator, a pressure-reducing valve, an after-cooler, a moisture separator and two check valves. It then flows through 3.81-cm-diam. copper tubing to the mixing tee and then into the test section.

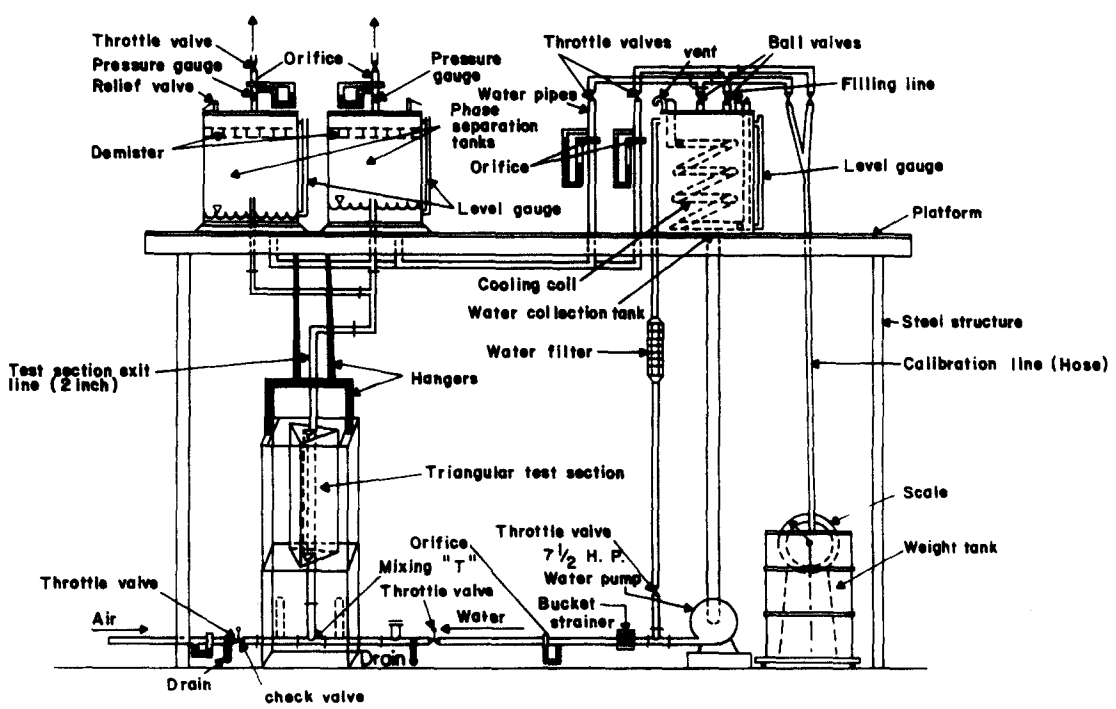

Figure 1. Air/water loop-water system.

The fluid exiting the test section was directed out through one of the parallel paths at the top and into one of the loop's air/water separator tanks. As shown in figure 1, these separator tanks were mounted on a platform above the test-section area.

After separation, the water exits from the bottom of the separator tanks. The exit lines from the separator tanks run parallel under the separator tanks, then up along the side of the water-collection tank. The water flow rate is metered with calibrated orifices and then is discharged into the collection tank, where it returns to atmospheric pressure.

After passing through a demister to remove moisture, the air, released from the top of the separation tanks, is metered with calibrated orifices and discharged outside the building.

The various flow rates are measured with six calibrated flange-tap orifice plates. As shown schematically in figure 1, these are located upstream of the various flow control valves. The resulting pressure differences across the orifice meters were measured with mercury-filled U-tube manometers. The flows thus measured are the inlet air, inlet water, and exit air and water flows from both separator tanks.

The orifice meters on the water side of the loop were calibrated using the standard-weight tank method. The air orifice meters, placed on the top of the separator tanks, were calibrated using the Pitot-tube method (i.e. the measured local velocities were integrated across the cross-section of the pipe to determine the total flow rate). The air orifice meter placed upstream of the test section was cross-calibrated by comparison with the orifices placed down stream of the test section.

Test section

The test section utilized for these phase-distribution experiments was a 91.44-cm-long isosceles triangle. The inside dimensions of the triangular test section are

- triangle height = 9.8425 cm,
- triangle base = 5.08 cm,
- apex angle = 29°,
- hydraulic diameter = 3.9395 cm.

The isosceles-triangular test section was cast from transparent plexiglass in order to permit visualization of the flow.

The case aluminum endpieces were designed to smoothly diffuse the two-phase mixture into the 91.44-cm-long test section. Numerous 1.59-mm-diam. ports were located along the apex of the triangle for instrumentation and/or for the introduction of air at various axial positions.

The triangular test section was equipped with a modified ball-valve fixture to introduce the probes at the apex of the triangle. Also, an angular-position indicator and a micrometer drive were used to properly position the probe within the flow field.

The detailed distribution of the void fraction was measured with a Radio Frequency (RF)-excited impedance probe and the liquid-phase velocity profile of the two-phase mixture was measured using a Pitot tube (Sim & Lahey 1983).

Pitot-tube measurement system

The dynamic pressure of the flow was measured using a Pitot tube and a variable reluctance differential-pressure transducer (Validyne DP-15). This transducer was designed for accurate low- and medium-differential-pressure measurements and could be used with different-range stainless steel diaphragms. Even though the linearity of the output voltage was guaranteed by the manufacturer, to ensure accuracy, the transducer was recalibrated after each change of diaphragm.

The output of the transducer was processed by a sine-wave carrier modulator (Validyne CD-15) with a dc output. This sine-wave carrier modulator operates in conjunction with the variable reluctance transducer to provide a dc output signal for dynamic, as well as steady state, measurements. A 5-kHz sine-wave excitation was applied to the two inductance-ratio arms of the transducer, and the resulting output was demodulated and amplified using an integrated-circuit technique. The dc output was obtained from an active low-pass filter circuit which gave a flat response from steady state to 1000 kHz.

The output voltage of the transducer was averaged over an interval of 3 min by an A/D converter-equipped microprocessor. The averaging time of 3 min was needed to get a statistically stationary reading. In addition, there was a requirement that the Pitot-tube lines should always be full of water (i.e. air bubbles in the lines create nonsteady erroneous signals). In order to insure this, a constant small-purge flow of water was circulated through the Pitot-tube lines. This flow was adjusted so as not to disturb the differential-pressure readings (i.e. to have the same pressure drop in each line).

As shown in figure 2, the valving manifold for the pitot tube was built and designed in such a way as to allow connection of the Pitot tube to the differential-pressure transducer; to determine the zero offset before each new Δp reading; to purge the piping system before each reading; to allow recalibration of the pressure transducer for each new diaphragm; and to be able to water purge the lines to assure that the lines were always full of water.

The Pitot tube was inserted into the test section through a modified ball valve and connected to a transversing mechanism (micrometer drive). The Pitot tube could be positioned at the measuring points in the test section using the micrometer feed and an angular indicator, which was attached to the test section.

The calibration of the differential-pressure transducer for each new diaphragm was made using two graduate titration columns which were connected to the upper-deck support columns. By adjusting the levels of the water in the columns, a known hydrostatic Δp could be applied to the transducer. For each diaphragm we determined the offset (zero), measured the Δp and the linearity of the signal. The necessary adjustments and offset settings were done using the zero and the span knobs placed on the carrier demodulator panel.

The Pitot-tube lines were always kept full of water using the purge line, which was connected down-stream of the main water-pump discharge. The purge pressure was about 4 bars. The tygon tubing used at the ends of the copper pipes allowed a visual check of all Δp lines. For each new recalibration, the transducer was purged using the purge fittings on the transducer. The maximum voltage given by the transducer was continuously checked

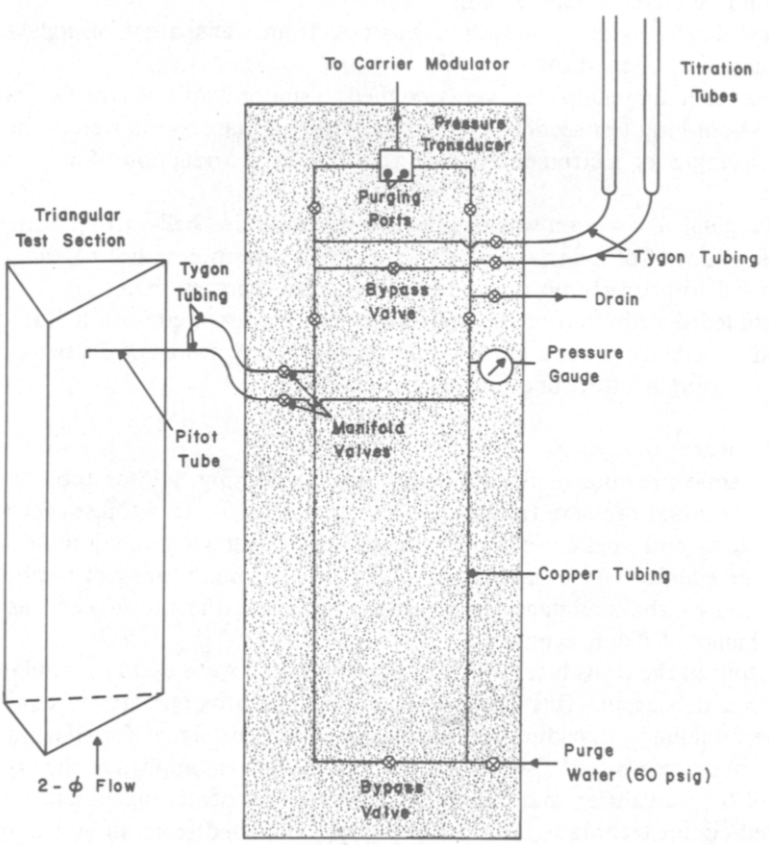

Figure 2. Pitot-tube measurement manifold.

on the digital voltmeter during the calibration and purging operations in order to ensure no damage to the diaphragm.

The Δp readings were inferred from the averaged voltages recorded on the teletype (the microprocessor output). The microprocessor was designed to give a zero-volt reading at $\Delta p = 0.0$ and 5 V at $\Delta p = \Delta p_{max}$. Due to the linearity of the signal, the calculation of the Δp, given the recorded voltage, came from the following linear correlation:

$$\Delta p = \frac{(V - V_0)}{(V_{max} - V_0)} \Delta p_{max} \quad , \qquad [1]$$

where,

Δp = the measured differential pressure,
V = voltage recorded on the teletype,
Δp_{max} = maximum range for the diaphragm used,
V_0 = offset voltage (corresponding to $\Delta p = 0.0$)
V_{max} = 5 V, maximum voltage output.

The measured time-averaged Δp were processed together with the local void fractions using several existing models for phase velocity. An overall continuity check was made to determine the validity of these models for out geometries and flow regimes.

RF impedance-probe measurement system

A Karlsruhe (KfK)-type local impedance probe was used to measure the local void fractions in the flow channel.

The probe has a stainless steel jacket. An inner stainless steel electrode is insulated from the jacket by alumina (Al_2O_3). The diameter of the probe was 0.7 mm to minimize flow-disturbance effects.

The Radio Frequency (RF)-excited probe was inserted into the test section through a modified ball valve and connected to the transversing mechanisms attached to the test section. The KfK probe was used as a capacitive element in variable-frequency oscillator (VFO) circuit. Polarization effects were eliminated as the probe tip was at ground potential. The difference in dielectric constant associated with each phase produced the needed phasic discrimination.

Since it was previously found (Vince & Lahey 1980) that derivative thresholding was superior to level thresholding, derivative thresholding was used to measure the local void fraction in the triangular test section.

A single-beam gamma densitometer system was employed as the standard against which to calibrate the local impedance probe. The local probe was calibrated to determine the appropriate derivative threshold setting.

Single-beam gamma densitometer system

Radiation attenuation is known to be the most reliable method to measure the chordal void fraction; thus a scanning single-beam gamma densitometer system was developed.

The principle behind such systems is well known. A collimated beam of photons from a radioactive source located outside of the test section is passed through the test section. The emerging beam was measured with a NaI scintillation detector on the opposite side of the test section. The attenuation of the beam depends on the amount of liquid intercepted by the beam. Thus photon beam attenuation can be directly related to the chordal-average void fraction. The chordal-average void fraction $\langle \alpha \rangle$, for a well-mixed two-phase flow is given by Schrock (1969), as

$$\langle \alpha \rangle = \frac{\ln(I/I_L)}{\ln(I_G/I_L)} \quad , \qquad [2]$$

where

I = intensity of a photon beam passing through a two-phase mixture in the test section (photons/m^2-s),
I_G = intensity of a beam passing through an air-filled test section (photons/m^2-s),
I_L = intensity of a beam passing through a water-filled test section (photons/m^2-s).

The source which was used in the gamma densitometer was a 5-Curie ^{137}Cs source. This was selected after considering the photon energy level, half-life, gamma abundance (fraction of decays which result in a photon emission) and the availability and cost of the various sources.

The accuracy desired was 1% (of point) in void fraction (i.e. $\Delta\langle\alpha\rangle/\langle\alpha\rangle = 0.01$) for the case of a steady air/water mixture flowing in the triangular test section. For the 5-Curie ^{137}Cs source used, the required counting time to achieve $\Delta\langle\alpha\rangle/\langle\alpha\rangle = 0.01$ was found from an analysis of the count statistics to be 10 min (Sim & Lahey 1983).

EXPERIMENTAL RESULTS AND DISCUSSION

Dynamic pressure

All dynamic-pressure measurements were done using a Pitot-tube measurement system. The measurement time was selected to be 3 min for each point.

The measurements were done first along the centerline ($\theta = 0°$) for the isosceles triangle at positions $X_i = (i/18)L_x$ using the transversing mechanism with the angle indicator set at $\theta = 0°$. In this expression, L_x is the height of the isosceles triangle and $i = 1,2,...,17$. After taking the center-line data, local transverse dynamic-pressure data were taken along chords parallel to the triangle's base by varying the angle indicator's position (i.e. $\theta = \pm 3°, \pm 6°, \pm 9°, \pm 12°$) at fixed X_i.

Since the Pitot tube had finite size, the data near the wall in apex region of the triangle could not be taken. Measurements were taken at two different flow rates and three different qualities, including single-phase liquid flow.

To better understand the dynamic-pressure distribution measured in the triangular test section, the measured data were plotted along the apex bisector of the triangle and different chords parallel to the triangle's base.

Figure 3 shows the dynamic pressure distribution along the triangle's apex bisector for low flow ($w = 1.682$ kg/sec) and various qualities, including single-phase liquid flow ($\langle x\rangle = 0.0\%$). It can be seen that the local Δp can go up as air is introduced, since the local dynamic head of the liquid phase increases. As more air is introduced, there is considerable lateral-phase separation, which results in a lower Δp in the interior of the conduit due to the high concentration of vapor there. Figure 4 shows the dynamic-pressure distribution for single-phase liquid flow (low flow) along seven different chords parallel to the triangle's base. As can be seen, in turbulent single-phase flow, along chords near the triangle's base, the dynamic pressure near the corners are somewhat higher than in the center due to secondary-flow effects.

Figures 5 and 6 show the expected data trends for low flow, at low quality ($\langle x\rangle = 0.257\%$) and at high quality ($\langle x\rangle = 1.1\%$), for various positions (x/L_x). As can be seen in figure 6, for high qualities, the Δp in the interior can be much lower than in the corner due to the annular-flow regime which existed. Figure 7 shows the Δp distribution along the triangle's apex bisector for high-flow rate ($w = 2.523$ kg/sec) and various qualities. For these high-flow conditions, annular flow does not occur even at the highest quality. Figures 8, 9 and 10 are similar plots for the high-flow case ($w = 2.523$ kg/sec) at $\langle x\rangle = 0.0\%$, $\langle x\rangle = 0.257\%$ and $\langle x\rangle = 1.1\%$, respectively.

These dynamic-pressure data must be combined with the corresponding local void-fraction data to determine the liquid-phase velocity distribution in the triangular test section.

Local void fraction

Local void fraction was measured for the same flow rates and qualities as those for the dynamic-pressure measurements. As discussed previously, derivative thresholding was employed using a RF-excited local impedance probe using derivative thresholding. Each

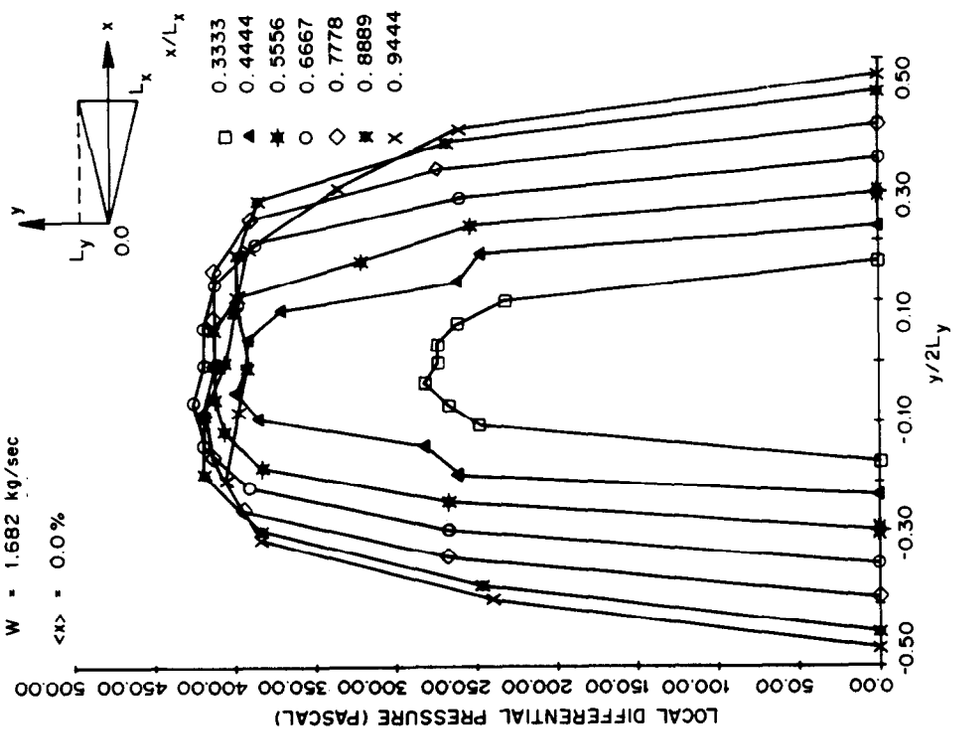

Figure 4. Plot of Δp distribution.

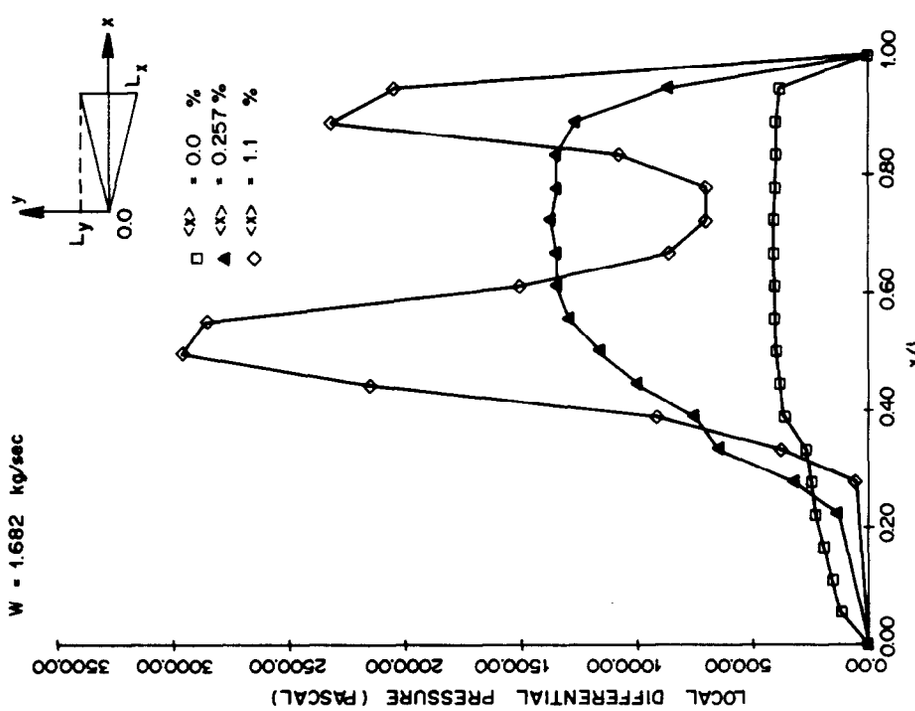

Figure 3. Plot of Δp distribution.

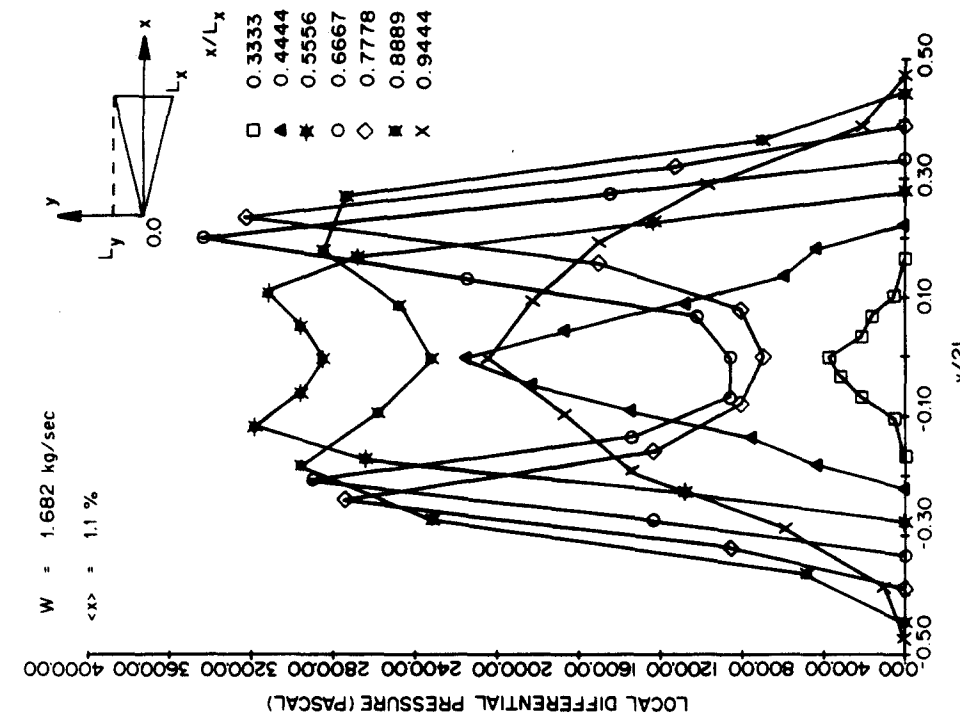

Figure 6. Plot of Δp distribution.

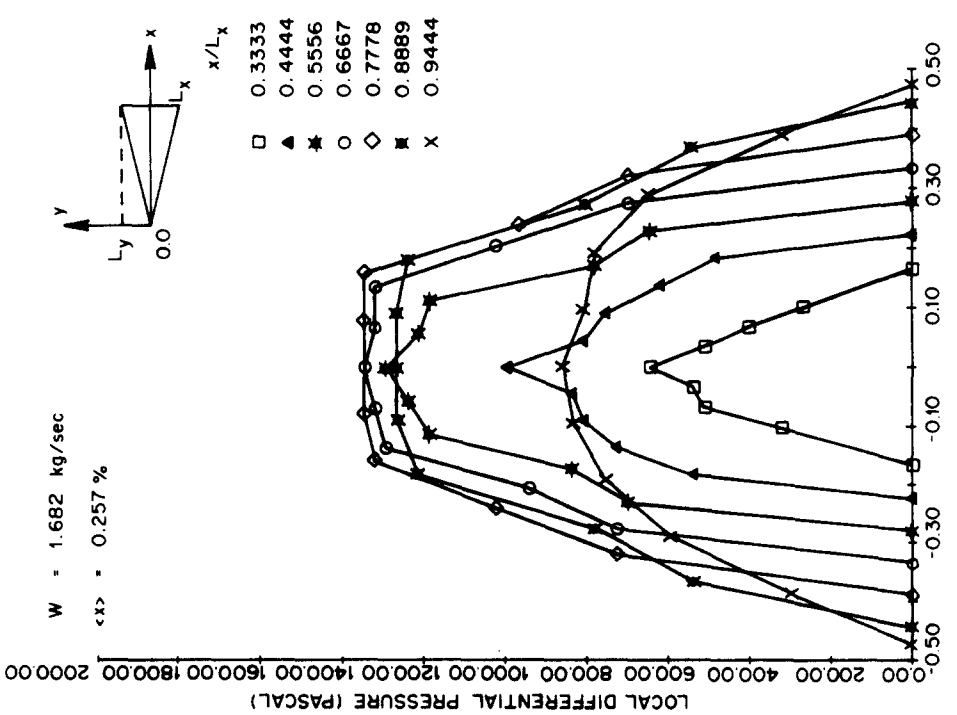

Figure 5. Plot of Δp distribution.

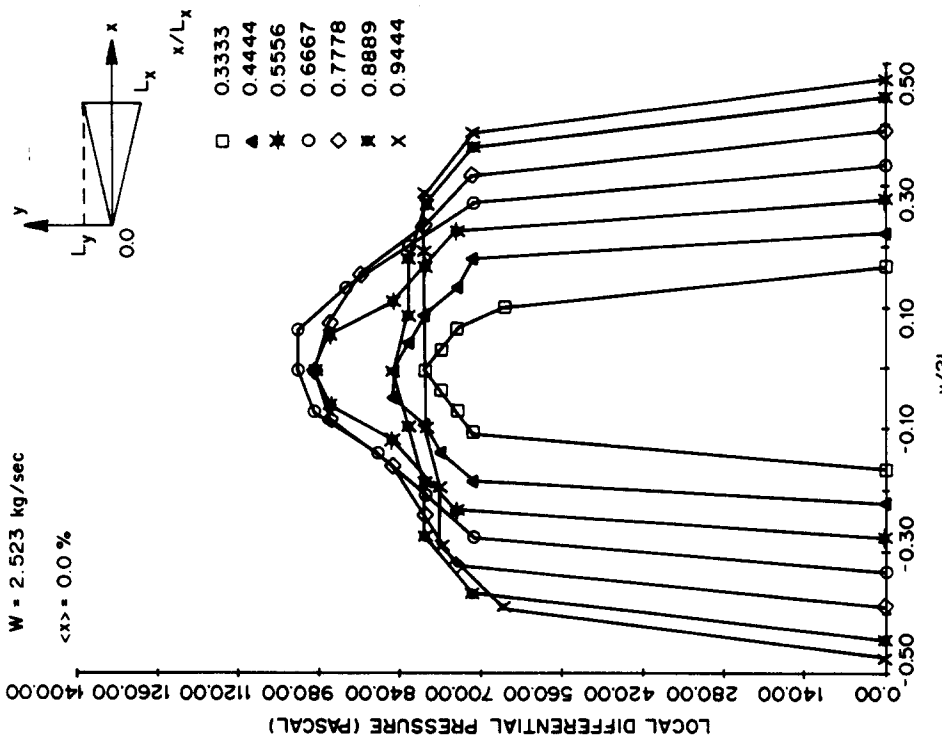

Figure 8. Plot of Δp distribution.

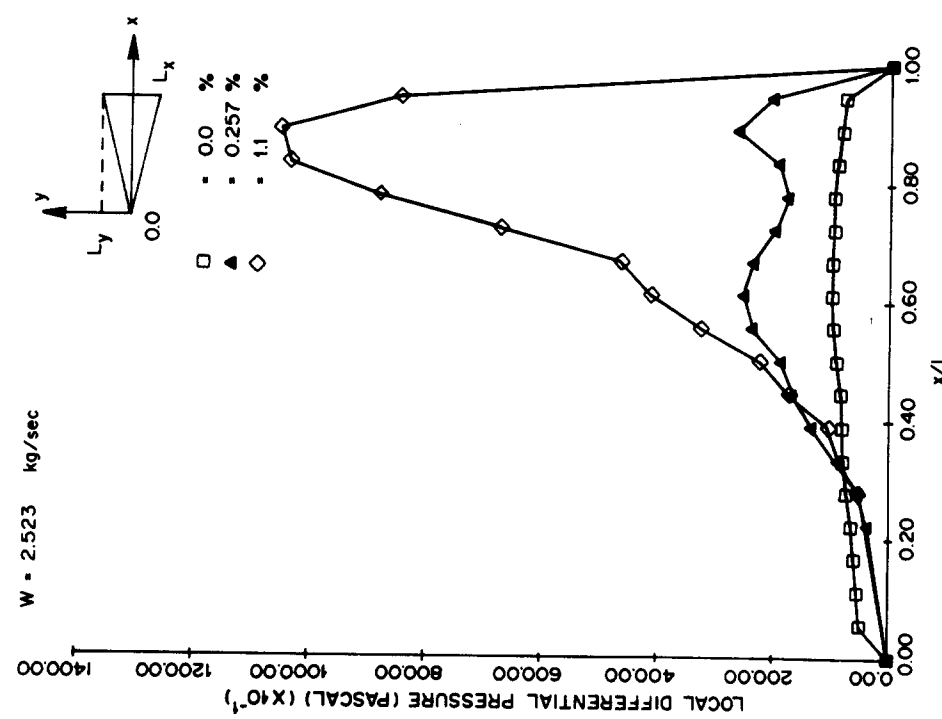

Figure 7. Plot of Δp distribution.

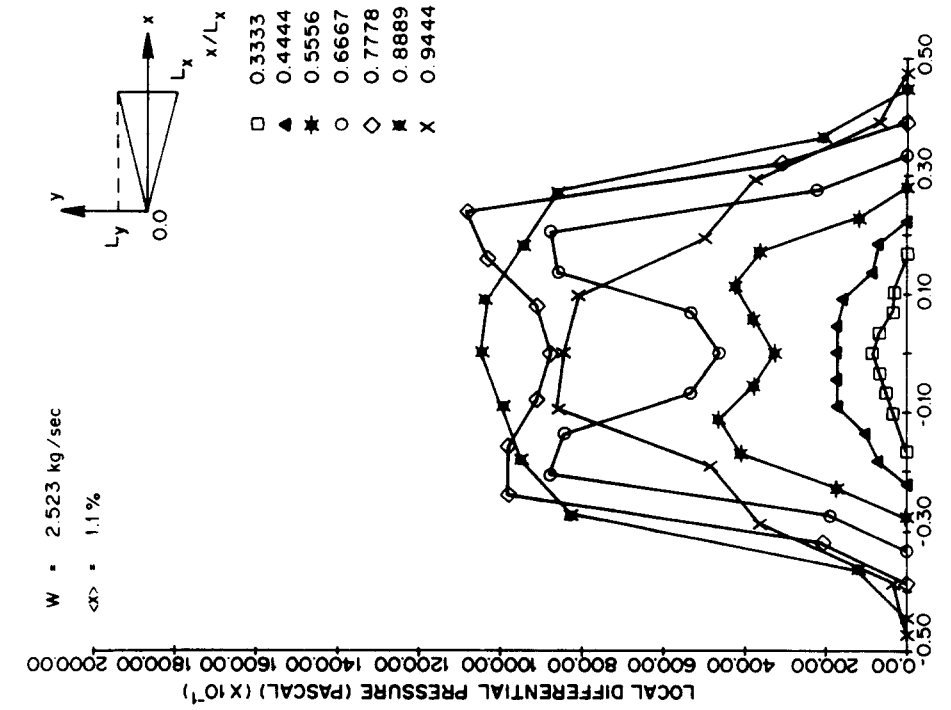

Figure 10. Plot of α distribution.

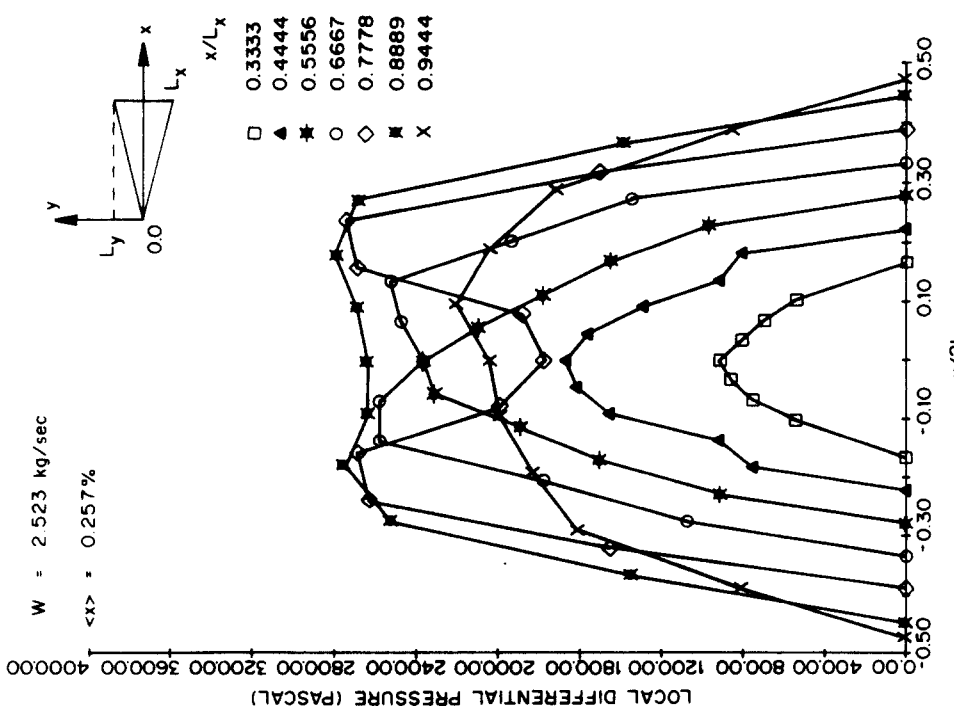

Figure 9. Plot of Δp distribution.

local void-fraction measurement was taken at the same measurement points that the dynamic pressure was taken at.

The measured local void-fraction data can be plotted in the same manner as the dynamic-pressure plots.

Figure 11 shows the local void distribution taken along the triangle's apex bisector for low flow, and both high and low qualities. It can be seen that the vapor tends to concentrate in the region of largest flow area. Figures 12 and 13 show void distribution in the test section for low quality and high quality, respectively. Visual observation indicated that the annular flow existed in the high-quality case. Figure 13 indicates pronounced lateral-phase distribution. Indeed, annular flow occurred in the region of largest flow area, while bubbly flow occurred near the apex of the triangle. Figures 14, 15 and 16 are similar plots for high-flow conditions. It was noted that churn-turbulent conditions appeared to exist in all cases of high flow. These data trends are consistent with the local dynamic-pressure distribution discussed previously.

In order to better appreciate the data trends, several runs have been replotted in a three-dimensional display in figures 17 and 18. The pronounced degree of lateral-phase separation can be easily seen.

Gamma-ray-measured chordal-average void fraction

Chordal-average void-fraction data were taken using a single-beam gamma densitometer system. The measurements were taken through chords parallel to the triangle's base at the same level that the local void-fraction data were taken (i.e. just below the tip of the local RF probe). These data were used as the standard for the local void-fraction data measured

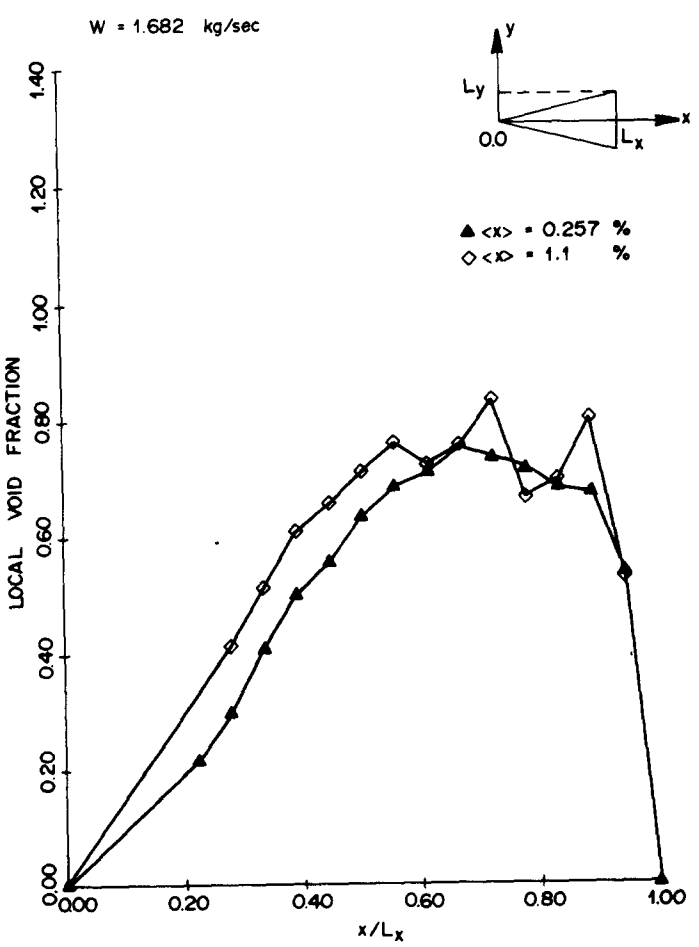

Figure 11. Plot of Δp distribution.

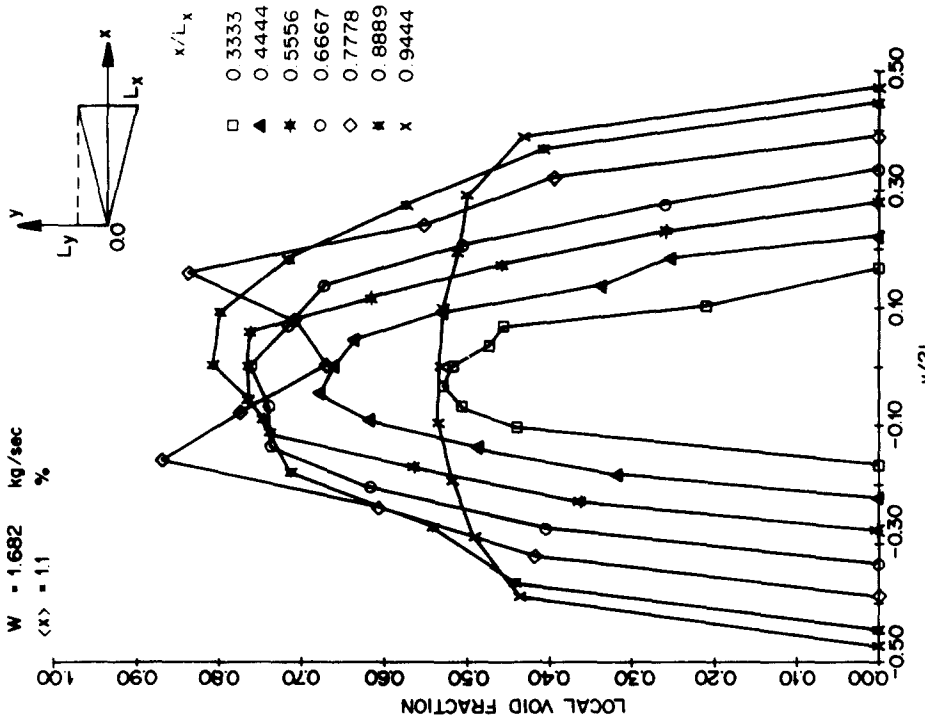

Figure 12. Plot of α distribution.

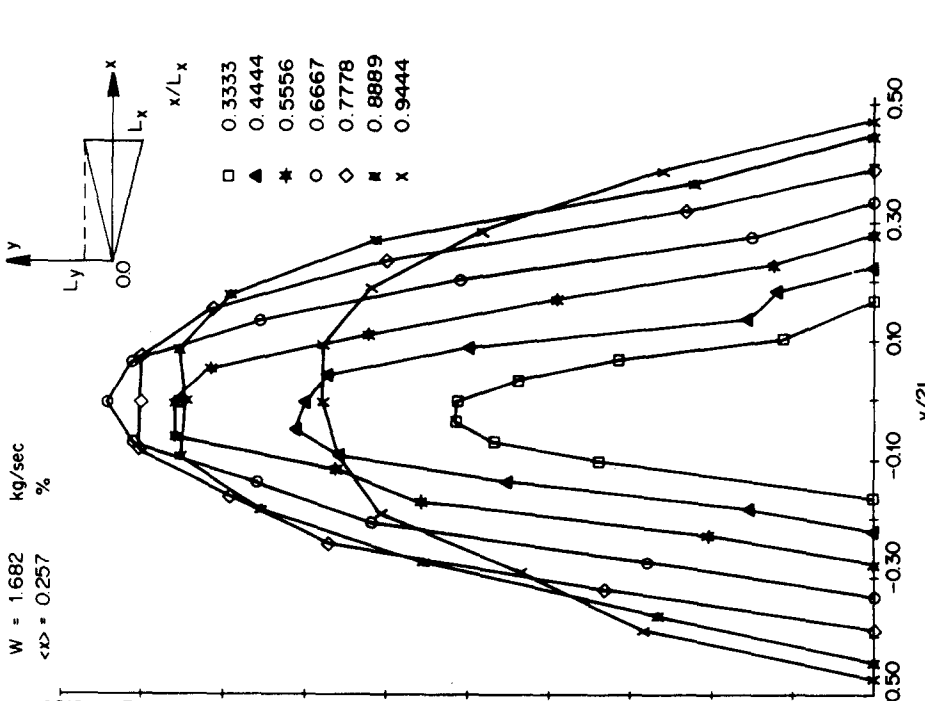

Figure 13. Plot of α distribution.

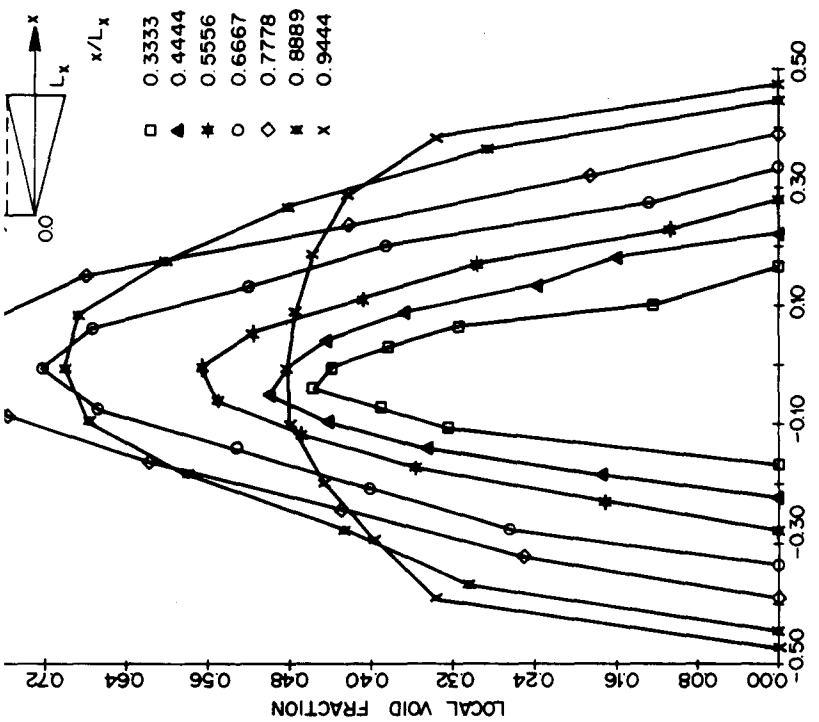

Figure 15. Plot of α distribution.

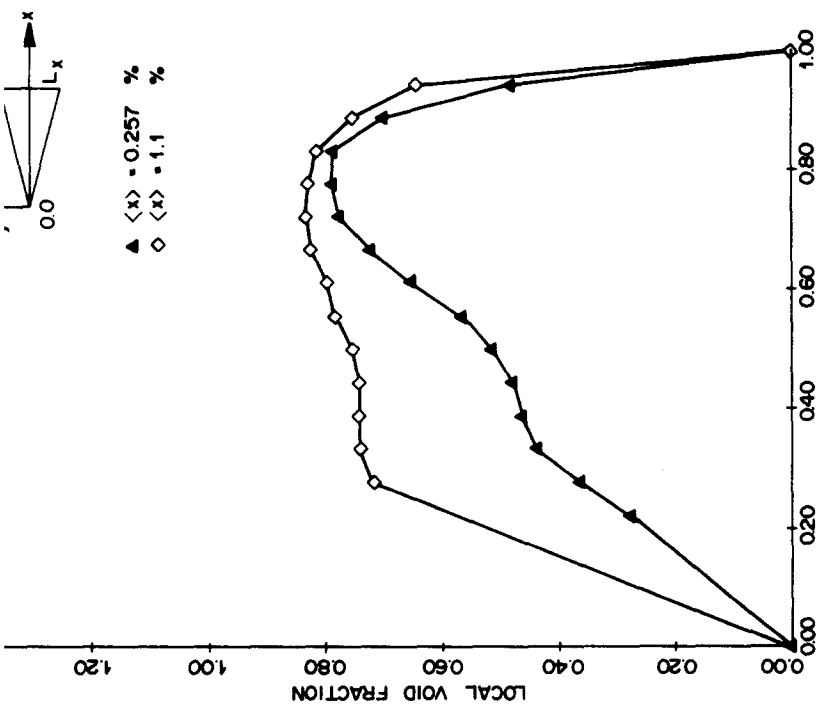

Figure 14. Plot of α distribution.

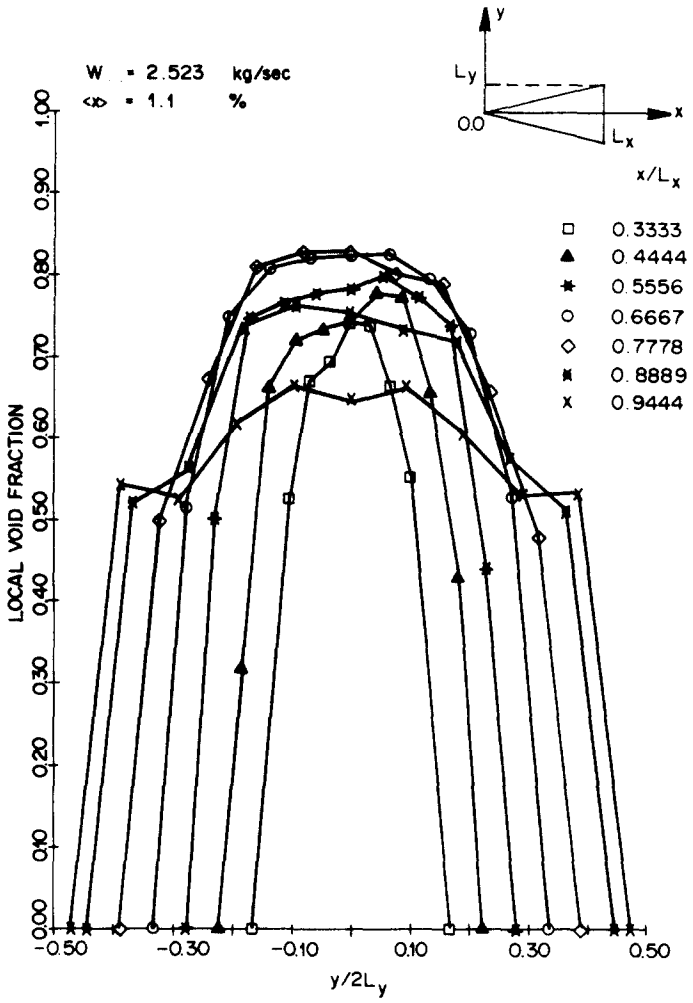

Figure 16. Plot of α distribution.

w = 1.682 kg/sec
<x> = 0.257 %

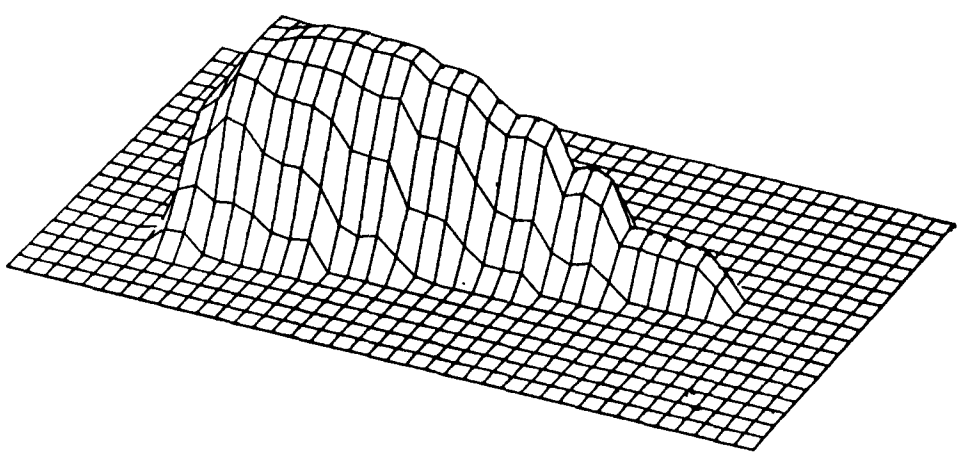

Figure 17. 3D plot for α distribution.

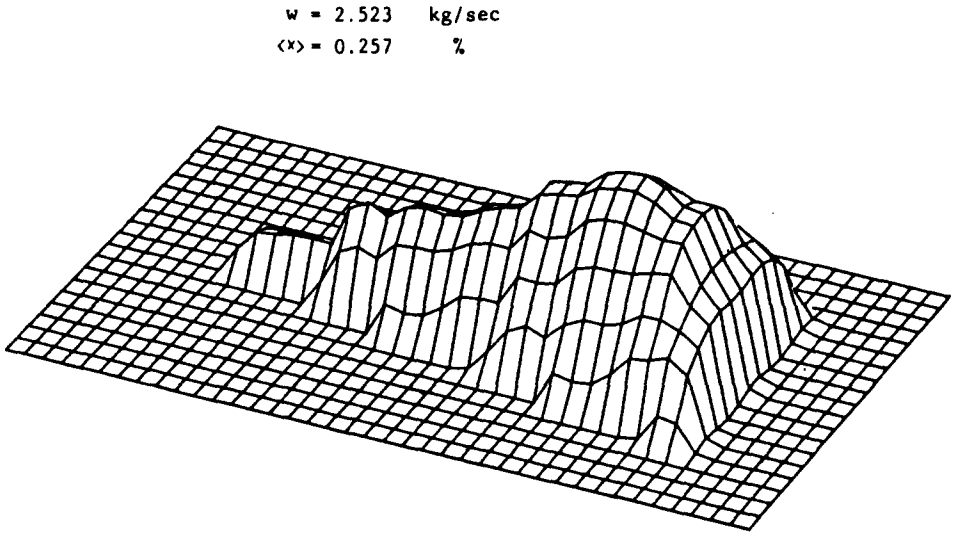

Figure 18. 3D plot for α distribution.

using the local RF probe. That is, these data were used for the calibration of the threshold setting of the local RF-excited impedance probe.

In order to compare the measured chordal-average void fraction to the calculated chordal-average void fraction, the local void-fraction data was numerically integrated to calculate the chordal-average void fraction, $\langle\alpha\rangle_{RF}$, using five-point nonuniform mesh Simpson's rule algorithm. Figures 19 and 20 show the comparisons between integrated chordal-average void fraction and the gamma-ray-measured chordal-average void fraction, $\langle\alpha\rangle_{\gamma}$, for low flow and high flow, respectively.

It can be seen that the agreement is good; however, for both flow cases; the high-quality, data gives somewhat better agreement than those for low quality due to the higher local liquid velocity in the channel (i.e. the higher the liquid velocity, the less the surface tension effects in the RF-probe data).

Local liquid-phase velocity

The local void-fraction data was combined with the local dynamic-pressure data to calculate local liquid-phase velocities and the total liquid-flow rate. The calculated total liquid-flow rates were used to determine the best local liquid-phase velocity data reduction model to use by a global continuity (of mass) check.

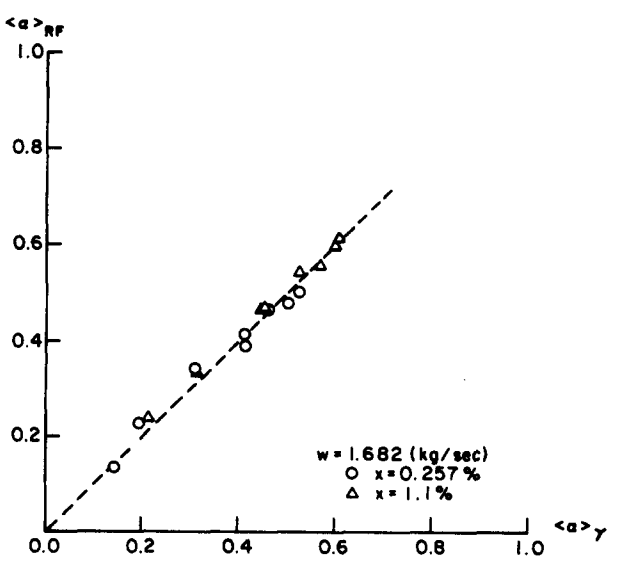

Figure 19. $\langle\alpha\rangle_{RF}$ vs $\langle\alpha\rangle_{\gamma}$ for low flow.

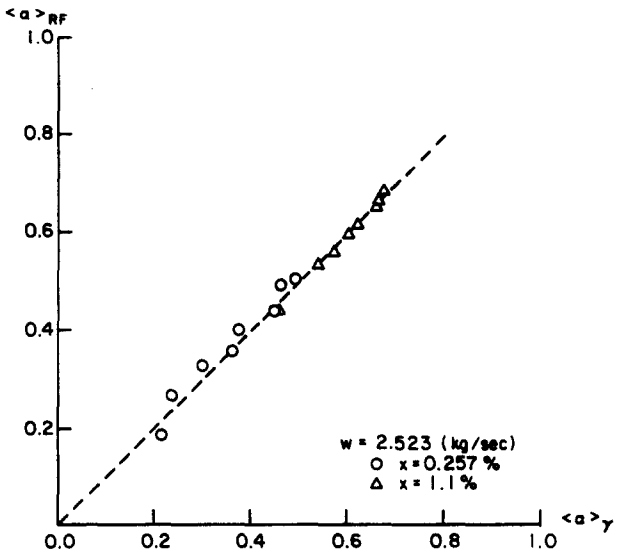

Figure 20. $\langle\alpha\rangle_{RF}$ vs $\langle\alpha\rangle_{\gamma}$ for high flow.

The local liquid-phase velocities previously discussed, were combined with the local void fractions at the same point and numerically integrated to calculate chordal-average superficial liquid velocities using a five-point nonuniform mesh Simpson's Rule algorithm. These chordal-averaged superficial liquid velocities were numerically integrated to calculate the cross-sectional-averaged liquid superficial velocity using the standard Simpson's rule algorithm for a uniform mesh. Finally, the total flow rate was calculated as

$$\overline{W}_L = \rho_L \langle v_L(1-\alpha)\rangle A_{x-s} \quad . \qquad [3]$$

The calculated total flow rates were compared with the measured flow rates. Various models for local liquid-phase velocity, tabulated in table 1, were tested in order to determine the model that gave the best overall continuity check with the data.

It was found that the Malnes model (1966) gave the best overall continuity check with the data, being within $\pm$ 6.3% for all runs.

Figures 21–28 show the local liquid-phase velocity distribution given by the Malnes model. Note that the single-phase (liquid)-velocity distributions are included in figures 21 and 25 for low and high flow, respectively.

SUMMARY AND CONCLUSIONS

In order to understand the multidimensional phase-distribution mechanisms, the local void-fraction and liquid-phase velocity were measured for fully developed, turbulent air/water flow through an isosceles-triangular duct using an RF-excited local impedance probe and Pitot tube, respectively.

Table 1. Liquid velocity data reduction models

$\alpha \triangleq$ local void fraction; $\rho_L \triangleq$ liquid density; $\Delta p \triangleq$ dynamic pressure	
Neal & Bankoff (1965) $\langle v_L\rangle = \frac{C}{4(1-\alpha)}\sqrt{\frac{2\Delta p}{\rho_L}}$ $C = 0.97$	Adorni (1961) $\langle v_L\rangle = \frac{1.0}{(1-\alpha)^2}\sqrt{\frac{2\Delta p}{\rho_L}}$
Walmet & Staub (1969) $\langle v_L\rangle = \frac{2}{(1-\alpha)(2+\alpha)}\sqrt{\frac{2\Delta p}{\rho_L}}$	Delhaye & Chevrier (1969) $\langle v_L\rangle = \sqrt{\frac{2\Delta p}{\rho_L}}$
Malnes (1966) $\langle v_L\rangle = \frac{1.0}{(1-\alpha)}\sqrt{\frac{2\Delta p}{\rho_L}}$	Bosio & Malnes (1969) $\langle v_L\rangle = \frac{1}{(1-\alpha/2)}\sqrt{\frac{2\Delta p}{\rho_L}}$

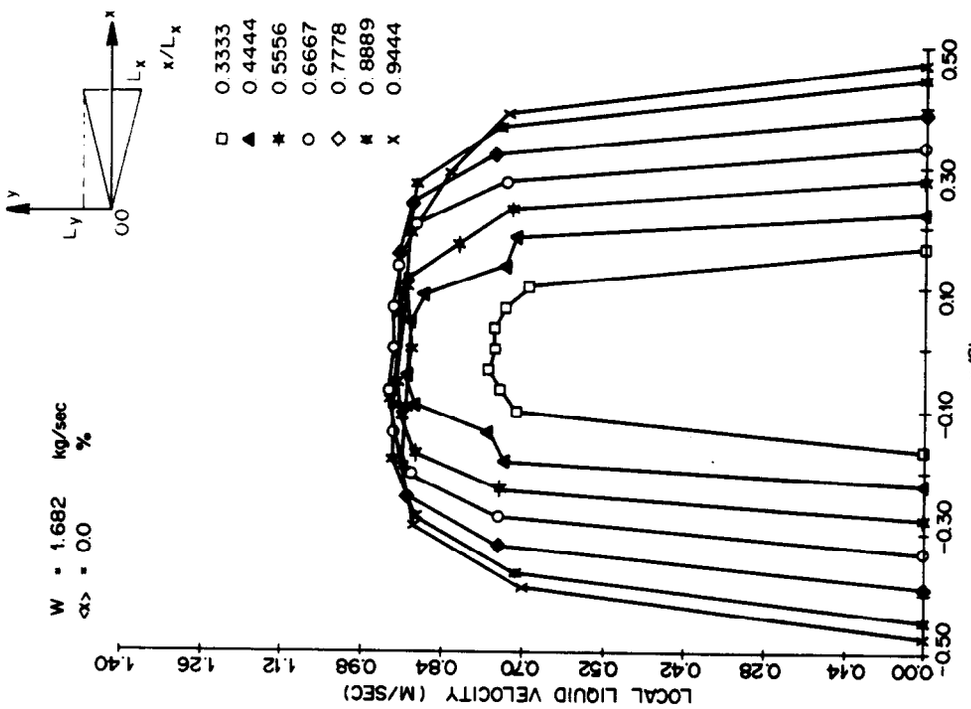

Figure 22. Plot of u_L distribution (using Malnes model).

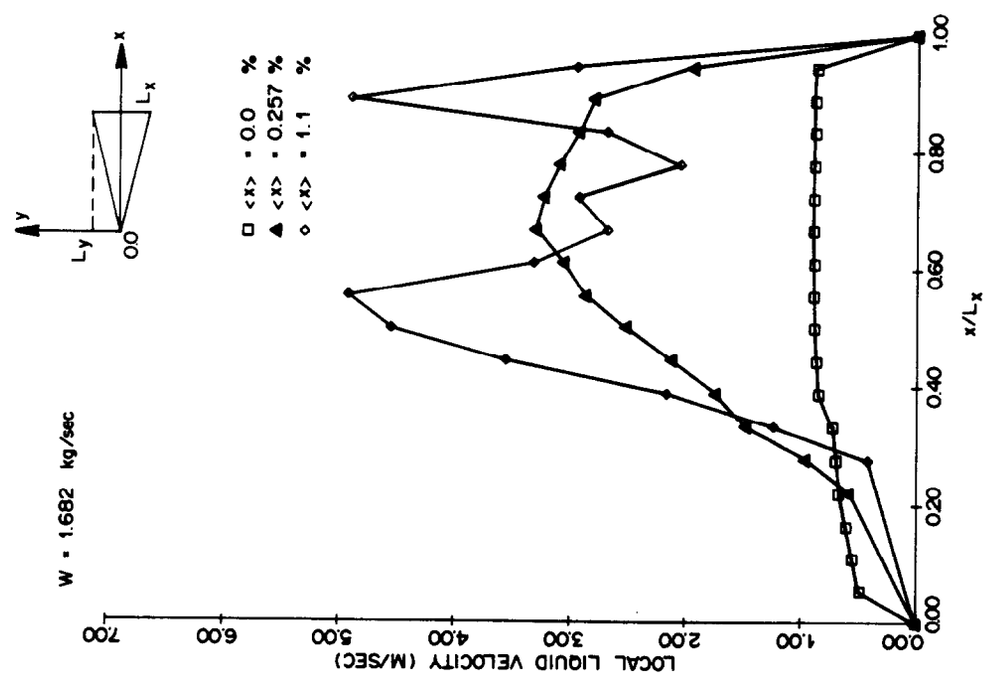

Figure 21. Plot of u_L distribution (using Malnes model).

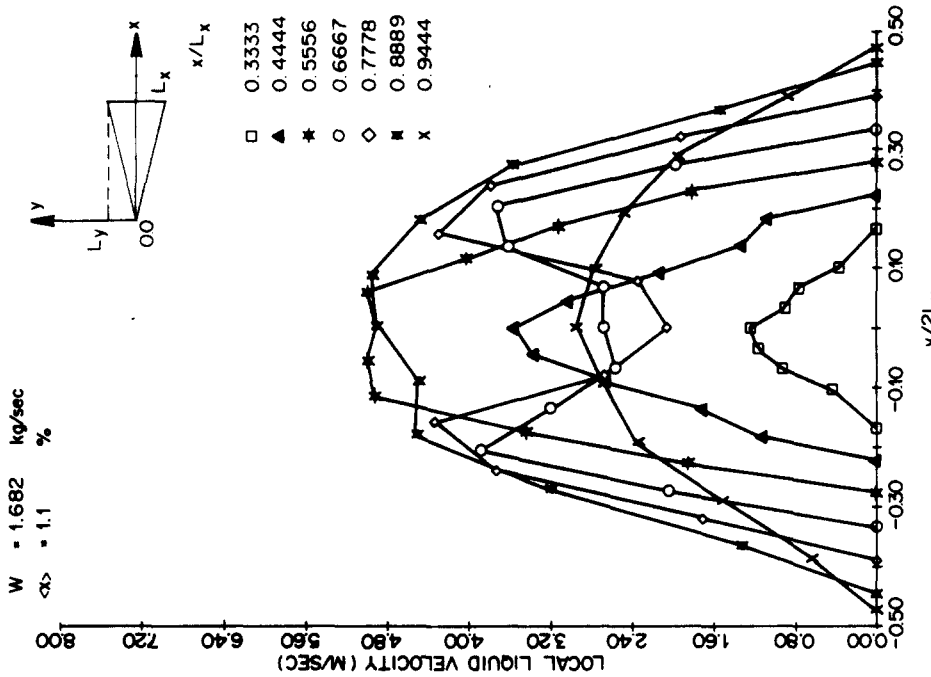

Figure 24. Plot of u_L distribution (using Malnes model).

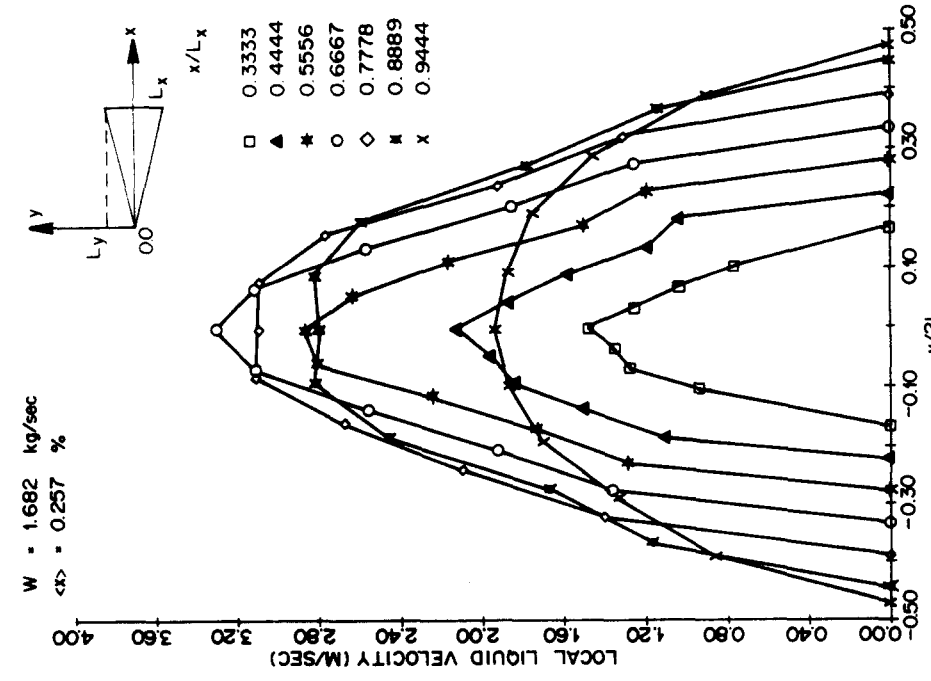

Figure 23. Plot for u_L distribution (using Malnes model).

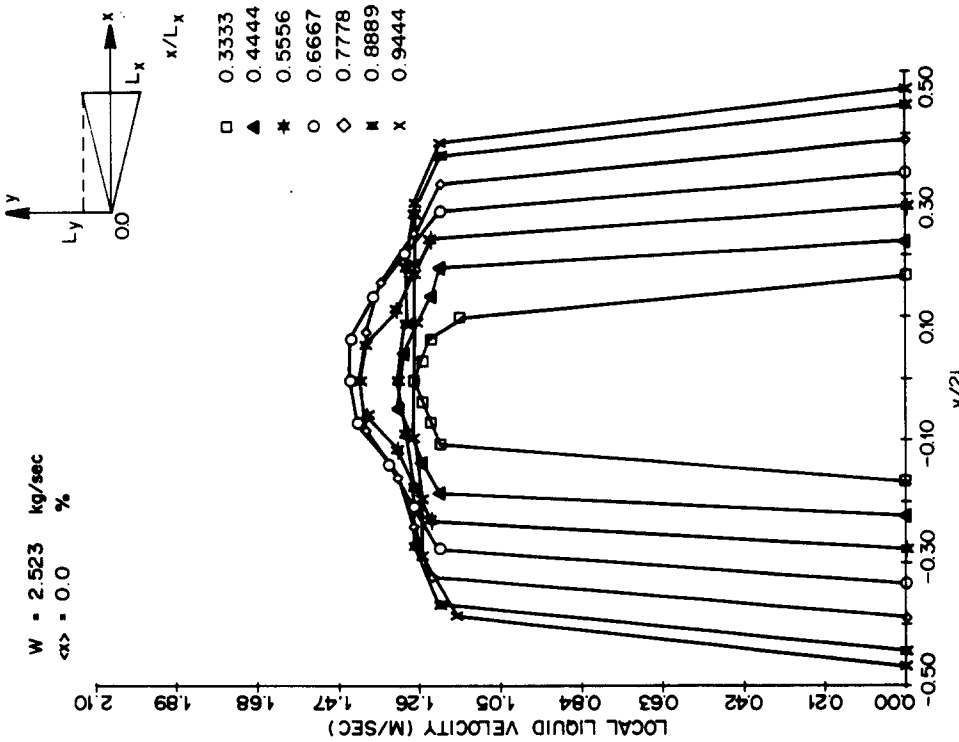

Figure 26. Plot of u_L distribution (using Malnes model).

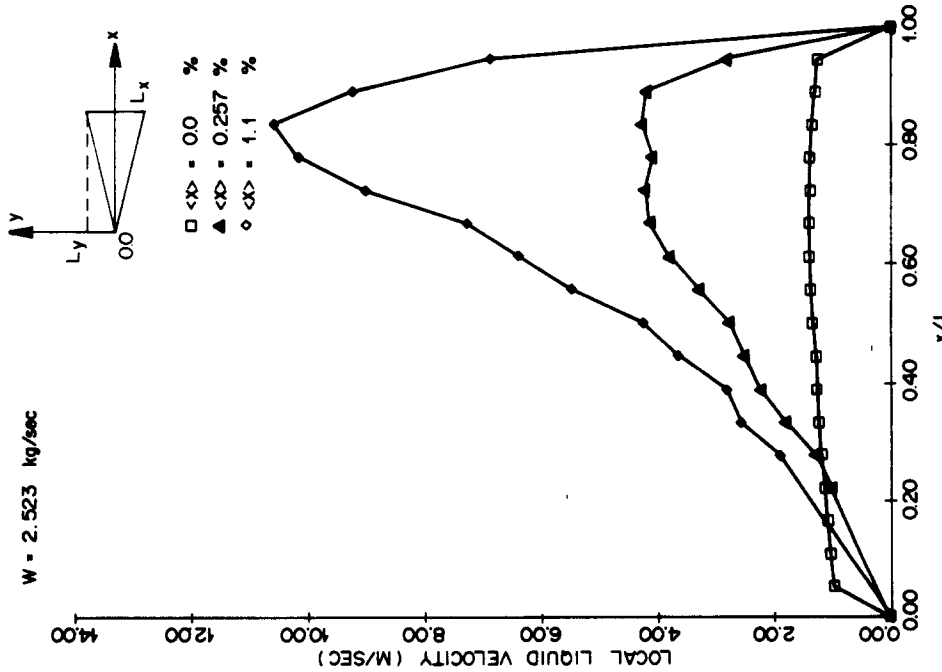

Figure 25. Plot of u_L distribution (using Malnes model).

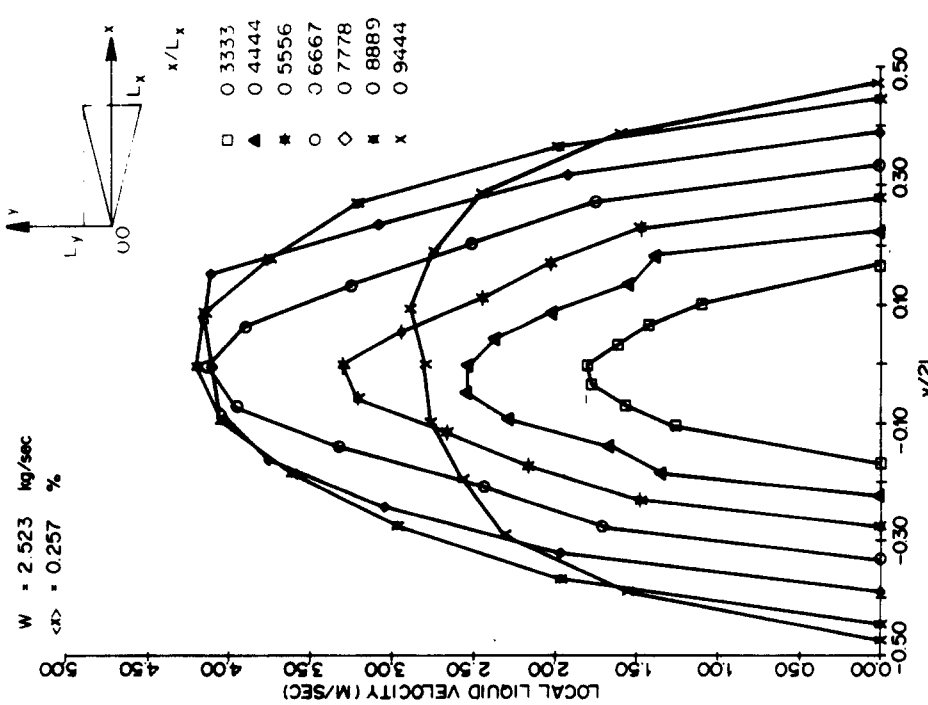

Figure 27. Plot of u_L distribution (using Malnes model).

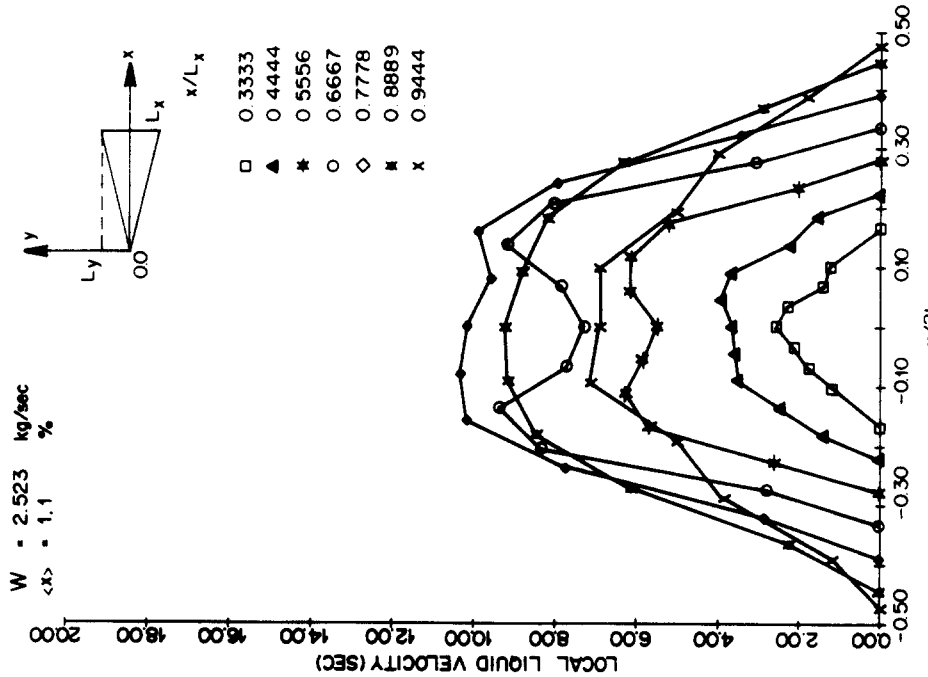

Figure 28. Plot of u_L distribution (using Malnes model).

The local void fraction was measured using a derivative threshold technique and a RF-excited local impedance probe. The measured local void-fraction data shows that the vapor tends to concentrate in the region of largest flow area. This is entirely consistent with previous data taken in more complex rod bundle geometries (Lahey *et al.* 1971).

The local void-fraction data was combined with the local dynamic-pressure data to evaluate the local liquid-phase velocities and the total liquid-flow rate. A global mass continuity check indicated that the model of Malnes (1966) gave the best overall continuity check with the data.

All the data taken indicated a pronounced degree of lateral-phase separation. Since it was not possible to take detailed turbulence distribution data with the instrumentation used, quantitative comparisons with the analytical model of Drew & Lahey (1981) were not possible. Nevertheless, excellent qualitative agreement with the model was found, since both the data and the model indicated that the vapor phase collects in the high-velocity regions of the test section. Since these data have been taken in a relatively simple geometry, they are considered to be ideally suited for the assessment of lateral "void-drift" models.

REFERENCES

ADORNI, N. 1961 Experimental data on two-phase adiabatic flow. CISE R35.

ALY, A. M. M., TRUPP, A. C. & GERRARD, A. D. 1978 Measurements and prediction of fully developed turbulent flow in an equilateral triangular duct. *J. Fluid Mech.* **85**, 57–83.

BEATTIE, D. R. H. 1972 Two-Phase Flow Structure and Mixing Length Theory. *Nucl. Engng Design* **21**, 46–64.

BOSIO, J. & MALNES, D. 1969 Water Velocity Measurements in Air/Water Mixture. Euromech Colloqium No. 7, Grenoble, France.

DELHAYE, J. M. & CHEVRIER, C. 1969 Comportement d'un Tube DePitot Dans Un Encoulment Eau-air A Grande Vitesse. CEA-Report-TT/69-9-B/JMDCC.

DREW, D. A. & LAHEY, R. T., JR. 1981 Phase distribution mechanisms in turbulent two-phase flow in channels of arbitrary cross section. *J. Fluid Engng* **103**, 583–589.

ECKERT, E. R. G. & IRVINE, T. F. 1956 Flow in corners of passages with noncircular cross sections. *Trans. ASME* **78**.

ISHII, M. 1975 *Thermo-Fluid Dynamic Theory of Two-Phase Flow*. Eyrolles, Paris.

LAHEY, R. T., SHIRALKAR, B. S. & RADCLIFFE, D. A. 1971 Mass flux and enthalpy distribution in a rod bundle for single and two-phase conditions. *J. Heat Transfer* **93**, 197–209.

LANCE, M., MARIE, J. L., CHARNAY, G. & BATAILLE, J. 1980 Turbulence structure of a co-current air/water bubbly flow. *Proc. ANS Meeting of Nuclear-Reactor Thermal Hydraulics*, Saratoga, NY, 1363–1383.

MALNES, D. 1966 Slip Ratios and Friction Factors in the Bubble Flow Regime in Vertical Tubes. Institute for Atomenergi, Kjeller, Norway, KR-110.

NEAL, L. G. & BANKOFF, S. G. 1965 Local parameters in cocurrent mercury-nitrogen flow. Parts I and II. *AIChE J.* **11**, 4.

NIKURADSE, J. 1926 Geschwindigkeitsverteilung in Turbulenten Stromungen. Zeitschrift-VDI, 70.

SCHROCK, V. W. 1969 Radiation attenuation techniques in two-phase flow measurement. ASME Symposium Volume, *Two-Phase Flow Instrumentation*, 24–35.

SERIZAWA, A. 1974 Fluid Dynamic characteristics of two-phase. Ph.D. thesis, Institute of Atomic Energy, Kyoto University, Japan.

SIM, S. & LAHEY, R. T. 1983 The Measurement of Phase Distribution Phenomena in a Triangular Conduit. NUREG/CR-3576.

VINCE, M. A. & LAHEY, R. T. 1980 Flow Regime Identification and Void Fraction Measurement Techniques in Two-Phase Flow. NUREG/CR-1962.

WALMET, G. E. & STAUB, F. W. 1969 Pressure, Temperature, and Void Fraction Measurement in Nonequilibrium Two-Phase Flow. ASME Symposium Volume, *Two-Phase Flow Instrumentation*, 89–101.